molecules

MDPI

Article

Design and Synthesis of Bisulfone-Linked Two-Dimensional Conjugated Microporous Polymers for CO_2 Adsorption and Energy Storage

Mohamed Gamal Mohamed [1,2,*], Siang-Yi Chang [1], Moshin Ejaz [1], Maha Mohamed Samy [1,2], Aya Osama Mousa [1] and Shiao-Wei Kuo [1,3,*]

[1] Department of Materials and Optoelectronic Science, College of Semiconductor and Advanced Technology Research, Center of Crystal Research, National Sun Yat-Sen University, Kaohsiung 804, Taiwan; shiang120321@gmail.com (S.-Y.C.)
[2] Chemistry Department, Faculty of Science, Assiut University, Assiut 71515, Egypt
[3] Department of Medicinal and Applied Chemistry, Kaohsiung Medical University, Kaohsiung 807, Taiwan
* Correspondence: mgamal.eldin34@gmail.com (M.G.M.); kuosw@faculty.nsysu.edu.tw (S.-W.K.)

Abstract: We have successfully synthesized two types of two-dimensional conjugated microporous polymers (CMPs), Py-BSU and TBN-BSU CMPs, by using the Sonogashira cross-coupling reaction of BSU-Br_2 (2,8-Dibromothianthrene-5,5′,10,10′-Tetraoxide) with Py-T (1,3,6,8-Tetraethynylpyrene) and TBN-T (2,7,10,15-Tetraethynyldibenzo[g,p]chrysene), respectively. We characterized the chemical structure, morphology, physical properties, and potential applications of these materials using various analytical instruments. Both Py-BSU and TBN-BSU CMPs showed high thermal stability with thermal decomposition temperatures (T_{d10}) up to 371 °C and char yields close to 48 wt%, as determined by thermogravimetric analysis (TGA). TBN-BSU CMPs exhibited a higher specific surface area and porosity of 391 $m^2\ g^{-1}$ and 0.30 $cm^3\ g^{-1}$, respectively, due to their large micropore and mesopore structure. These CMPs with extended π-conjugated frameworks and high surface areas are promising organic electroactive materials that can be used as electrode materials for supercapacitors (SCs) and gas adsorption. Our experimental results demonstrated that the TBN-BSU CMP electrode had better electrochemical characteristics with a longer discharge time course and a specific capacitance of 70 F g^{-1}. Additionally, the electrode exhibited an excellent capacitance retention rate of 99.9% in the 2000-cycle stability test. The CO_2 uptake capacity of TBN-BSU CMP and Py-BSU CMP were 1.60 and 1.45 mmol g^{-1}, respectively, at 298 K and 1 bar. These results indicate that the BSU-based CMPs synthesized in this study have potential applications in electrical testing and CO_2 capture.

Keywords: dibenzo[g,p]chrysene; conjugated microporous polymers; Sonogashira–Hagihara coupling reaction; CO_2 capture; supercapacitors

Citation: Mohamed, M.G.; Chang, S.-Y.; Ejaz, M.; Samy, M.M.; Mousa, A.O.; Kuo, S.-W. Design and Synthesis of Bisulfone-Linked Two-Dimensional Conjugated Microporous Polymers for CO_2 Adsorption and Energy Storage. *Molecules* **2023**, *28*, 3234. https://doi.org/10.3390/molecules28073234

Academic Editor: Lihua Gan

Received: 12 March 2023
Revised: 29 March 2023
Accepted: 1 April 2023
Published: 4 April 2023

1. Introduction

While digital life brings comfort, it also presents difficulties that people must consider. This energy source and storage support the advent of electronic products, and the energy relies primarily on the supply of the natural environment [1–7]. Renewable energy sources include solar and wind power, ocean energy, hydropower, and biomass; limited energy sources come from industrial fossil fuels such as coal, natural gas, and oil [8–15]. The pursuit of green environmental protection without affecting the life experience of most consumers, or how to ensure the supply and demand of energy while improving economic effects, is a heavy part of technology today. An increasingly well-known energy storage device to deal with this situation is the supercapacitor (SC), which has been studied since the 19th century [16–25]. SCs were developed for the same purpose as secondary batteries and conventional capacitors. They are all used for the convenience of energy storage, but supercapacitors have fewer limitations and wider prospects than the other two [26–30].

For example, its excellent reaction kinetics, higher power density, and gradually improved energy density make it more suitable for charging and discharging [26–30]. In addition, the improved cycle life and wider operating range of SCs allow them to operate stably and continuously [31–35]. Currently, it has achieved practical penetration in many fields, including mobile wearable devices, smart electronic appliances, electric transportation vehicles, medical treatment, and the defense industry [36–40]. SCs can be preliminarily divided into electric double-layer capacitors (EDLCs), pseudocapacitors (PCs), and hybrid supercapacitors (HSCs) based on their charge storage mechanism [36–40]. The energy storage principle of EDLCs focuses on electrostatic adsorption between the electrodes and electrolytes. EDLCs are highly efficient and reversible owing to their charge-physical adsorption behavior. Nevertheless, decisive factors concerning the reactivity of electrochemical capacitors are the properties of the electrolyte and electrodes [41–50]. The electrode materials used in EDLCs are primarily metal oxides, carbon-based materials, or conducting polymers [51–59]. We have investigated many modifications based on the molecular design or synergistic effects of conducting polymers to enhance their competitiveness in the market.

Among these, covalently linked and highly cross-linked conjugated microporous polymers (CMPs) are suitable for this concept [60–64]. The structural diversity of π systems and chemically reactive groups coupled with chemical stability and electrical conductivity are attractive advantages of CMPs. Specifically, a framework rich in micropores contributes to excellent surface conditions [60–64]. On this premise, the introduction of thianthrene-5,5′,10,10′-tetraoxide as a matrix in CMP enhances charge injection/transport performance and inter-bond interactions [65,66]. This group is beneficial for making the sample highly rigid [65,66]. In contrast, the participation of aromatic systems in Py-T and TBN-T units improves the conjugation properties of the materials. The pyrene contained in the former structure was connected by four benzene rings, which facilitated π-π stacking. The distribution of electrons exhibited by this state has led to great progress in the conduction performance of organic electrochemical substances. Under these circumstances, the continuous conjugated structure of the pyrene molecule can also reduce steric hindrance and change the flexibility of the chain [67–71]. For the same reason, TBN-T was chosen as one of the backbones in another CMP synthesis reaction. The TBN structure of the monomer center is upgraded to be connected by six benzene rings, which can improve the electrical properties of the material without sacrificing the rigidity of the material [72–74]. This has a positive effect on SCs.

In summary, we believe that BSU CMPs, with practical connotations, are highly feasible to become a potential stock for emerging developments. We believe that this is the first investigation into CMP materials with a bisulfone (BSU) moiety for applications involving gas uptake and energy storage. Herein, a facile and efficient Sonogashira cross-coupling reaction was used to construct and prepare two 2D-CMP-containing bisulfone moieties in high yields (Py-BSU and TBN-BSU CMPs) by the reaction of brominated thianthrene-5,5′,10,10′-tetraoxide with different ethynylpyrene (Py-T) and ethynyldibenzo[g,p]chrysene (TBN-T) molecules in DMF/Et_3N as solvents and Pd catalysts (Scheme 1). Solid-state NMR (ssNMR) and FTIR investigations supported the formation of Py-BSU and TBN-BSU CMPs, and PXRD, BET, SEM, EDS-SEM mapping, TEM, and TGA also investigated their morphology and porosity. Due to their good properties, such as high thermal stability, extended π-conjugated frameworks, and good BET surface areas, these materials are applied in CO_2 capture and supercapacitors applications. The electrochemical experiments show that the Py-BSU CMP and TBN-BSU CMP electrodes in the three-electrode system exhibited specific capacitances of 38 and 70 F g^{-1}, respectively, and an excellent capacitance retention rate of up to 99% in the 2000-cycle stability test. Furthermore, the TBN-BSU CMP sample exhibited high CO_2 uptake (1.60 mmol g^{-1}) due to the high surface area, pore volume, and tunable pore size of TBN-BSU CMP. According to these results, the BSU-based CMP prepared in this study has novel and accessible application potential in gas adsorption and electrical testing.

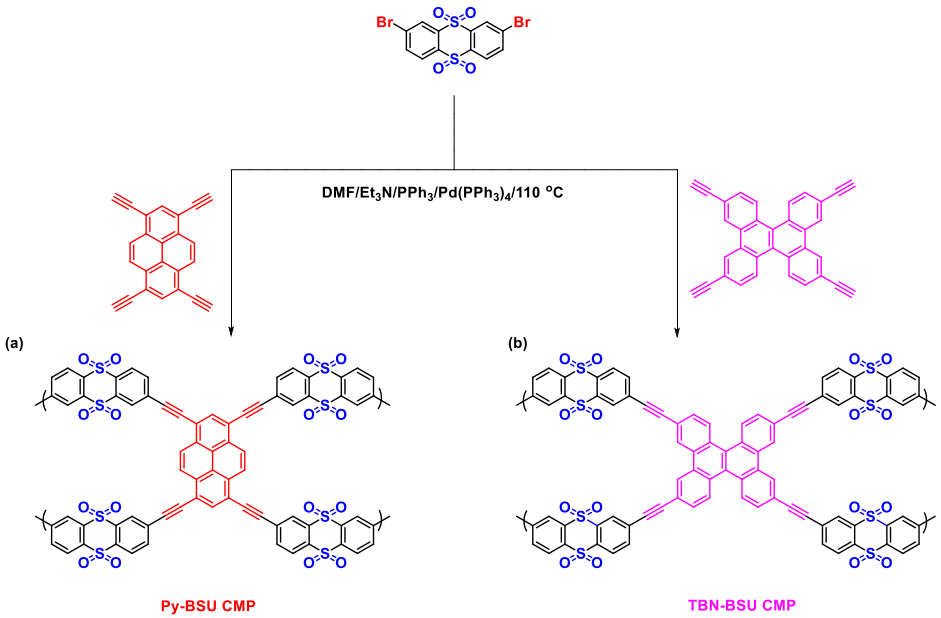

Scheme 1. Synthetic route for (**a**) Py-BSU CMP and (**b**) TBN-BSU CMP.

2. Results and Discussion

2.1. Synthesis and Characterization of Synthesized Monomers, Py-BSU and TBN-BSU CMPs

The BSU-Br_2 monomer was prepared in two steps. The THT molecule was brominated in a neat Br_2 solution in AcOH to afford THT-Br_2 as a white solid (Scheme S1). THT-Br_2 was then reacted with H_2O_2 solution in AcOH solution at 90 °C to produce BSU-Br_2 as a white solid (Scheme S2). The FTIR pattern of BSU-Br_2 (Figure S4) showed peaks at 3064 cm^{-1} for the aromatic rings and 1171 cm^{-1} for the SO_2 group, indicating the successful formation of BSU-Br_2 from THT-Br_2. Furthermore, the ^1H and ^{13}C NMR data confirmed the chemical structure of BSU-Br_2 (Figures S5 and S6). The FTIR and NMR results for other synthesized monomers in this study, such as THT-Br_2, Py-Br_4, Py-TMS, Py-T, TPE, TPE-Br_4, TBN-Br_4, and TBN-TMS, have been provided and discussed in detail in the experimental section (Figures S1–S3 and S7–S25). The signals at 3279, 3065, 2186, and 1618 cm^{-1} are attributed to the absorption characteristics for ≡C–H, aromatic C–H, C≡C, and C=C stretching in the Py-T structure (Figure S11). The ^1H NMR pattern (Figure S12) of Py-T peaked at 8.68, 8.38, and 3.67 ppm, corresponding to the phenyl and alkynyl groups, respectively. In addition, the aromatic carbon resonances appeared in the range 133.80–127.80, 84.50, and 82.00 ppm in the ^{13}C NMR spectrum (Figure S13) of Py-T due to the presence of aromatic and alkynyl units. As shown in Schemes S5–S7, there were three steps during the preparation of the TBN-T monomer. In dry nitromethane and DCM, TPE-Br_4 was reacted with anhydrous $FeCl_3$ to produce a yellow powder of TBN-Br_4. To prepare TBN-TMSA, a TBN-Br_4 precursor was combined with (trimethylsilyl)acetylene (TMSA) in the presence of CuI with diethylamine as the solvent. The treatment of TBN-TMSA with K_2CO_3 in methanol and DCM to produce a yellow solid allowed for the effective synthesis of TBN-T. The peaks in the FTIR spectrum of TBN-T (Figure S26) at 3291, 3057, 2106, and 1604 cm^{-1} were attributed to C≡C-H, aromatic C-H, C≡C, and C=C stretching, respectively. The proton signal was observed in the ^1H NMR spectra of TBN-T (Figure S27) at 3.30 ppm for C≡C-H. In addition, the presence of aromatic rings and C≡C units in the TBN-T compound caused carbon peaks at 135.70–101.60, 84.21, and 78.87 ppm, as seen in the ^{13}C-NMR spectrum (Figure S28).

As shown in Scheme 1, Py-BSU CMP (Scheme 1a) and TBN-BSU CMP (Scheme 1b) were prepared by reacting BSU-Br_2 with Py-T and TBN-T in a mixture of DMF/Et_3N for 3 days to afford dark red powder for Py-BSU CMP and yellow solid for TBN-BSU CMP. The solubility test in different organic solvents (NMP, DMSO, DMF, MeOH, EtOH, DCM,

and THF) revealed the insolubility of these materials compared to their corresponding monomers (BSU-Br_2, Py-T, and TBN-T) and confirmed that both BSU-CMP frameworks had a high cross-linking density. The chemical characteristics of Py-BSU and TBN-BSU CMPs were identified by Fourier transform infrared spectroscopy and solid-state ^{13}C nuclear magnetic resonance spectroscopy (ssNMR). A schematic of the corresponding structure is shown in Figure 1a. The absorption bands in Py-BSU CMP and TBN-BSU CMP around 3070 and 1580 cm^{-1} in the FTIR profiles (Figure 1b) measured at room temperature revealed the stretching of C-H and C=C in aromatic units, and the stretching absorption band of the C≡C bond appeared at 2200 cm^{-1}. The appearance of absorption bands centered at 1167 cm^{-1} for Py-BSU CMP and 1177 cm^{-1} for TBN-BSU CMP corresponds to the SO_2 unit in their framework (Figure 1b). The broad peaks at 95–115 ppm in the ssNMR spectra (Figure 1c) represent the signals of aromatic carbon atoms in the Py-BSU CMP and TBN-BSU CMP structures. Internal -C≡C- units in both Py-BSU CMP and TBN-BSU CMP were centered at 74.80 and 64.04 ppm, respectively [75–77]. The above results confirmed that Py-BSU CMP and TBN-BSU CMP were successfully constructed through a coupling reaction. In addition, the thermogravimetric analysis (TGA) in Figure 1d and Table 1 demonstrates the good thermal stability of the BSU-CMP materials under a nitrogen atmosphere, which is due to the high degree of cross-linking of the BSU-CMP materials after the Sonogashira cross-coupling reaction. The 5% weight loss (T_{d5}) of Py-BSU CMP and TBN-BSU CMP occurred at 320 and 338 °C, 10% weight loss (T_{d10}) of Py-BSU CMP and TBN-BSU CMP occurred at 383 and 386 °C, respectively, and the char yields at 800 °C were 48 and 56 wt%, respectively.

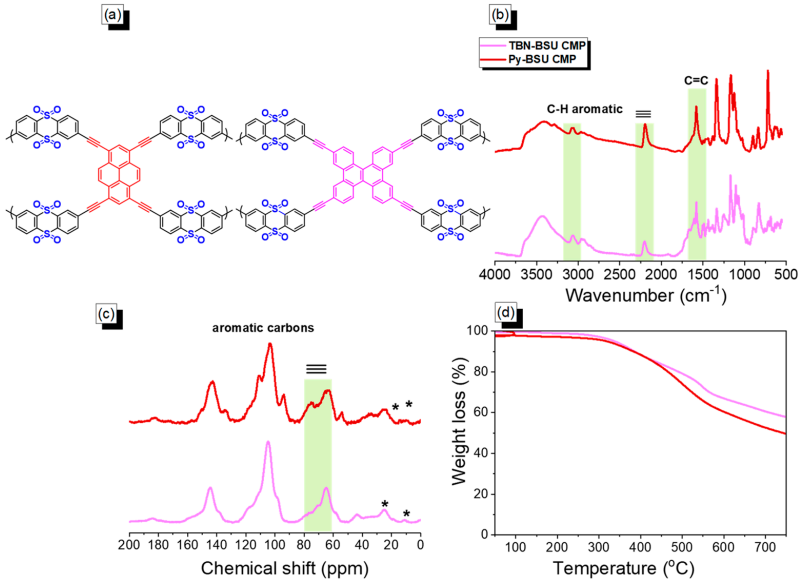

Figure 1. (**a**) Schematic diagram. (**b**) FTIR spectra, (**c**) SSNMR, and (**d**) TGA curves of Py-BSU CMP and TBN-BSU CMP. * the side band of solid-state nuclear magnetic resonance spectroscopy (NMR).

Table 1. Thermal stabilities and porosity properties of Py-BSU CMP and TBN-BSU CMP.

Sample	T_{d5} (°C)	T_{d10} (°C)	Char Yield (wt.%)	S_{BET} (m^2 g^{-1})	Pore Volume (cm^3 g^{-1})	Pore Size (nm)
Py-BSU CMP	320	383	48	42	0.07	2.57
TBN-BSU CMP	338	386	56	391	0.30	1.80

The porosity behavior of Py-BSU CMP and TBN-BSU CMP was determined using the Brunauer-Emmett-Teller (BET) theory, and the specific surface area and pore characteristics were confirmed through nitrogen adsorption/desorption analysis at 77 K. Both Py-BSU CMP and TBN-BSU CMP were vacuum degassed at 150 °C for 8 h to eliminate the huge

effect caused by water and other gases in the gas adsorption experiment. According to the IUPAC classification, the Py-BSU CMP in Figure 2a exhibits a type V isotherm with H_2 hysteresis loops that reflect typical ink bottle holes with uneven pore size distributions or close-packed interstitial pores of spherical particles. While TBN-BSU CMP in Figure 2b exhibits a type I isotherm with an H_1 hysteresis loop, the surge in the region of low relative pressure (<0.02) confirms that this material has a large number of micropores. The specific surface areas of Py-BSU CMP and TBN-BSU CMP were 42 and 391 $m^2\ g^{-1}$. Their corresponding total pore volumes are 0.07 and 0.30 $cm^3\ g^{-1}$, respectively. In addition, we estimated the pore size distribution (PSD) of Py-BSU CMP and TBN-BSU CMP from the N_2 adsorption isotherm using the nonlocal density functional theory (NLDFT). The results show that the average pore diameters of Py-BSU CMP (Figure 2c) and TBN-BSU CMP (Figure 2d) were approximately 2.57 and 1.80 nm.

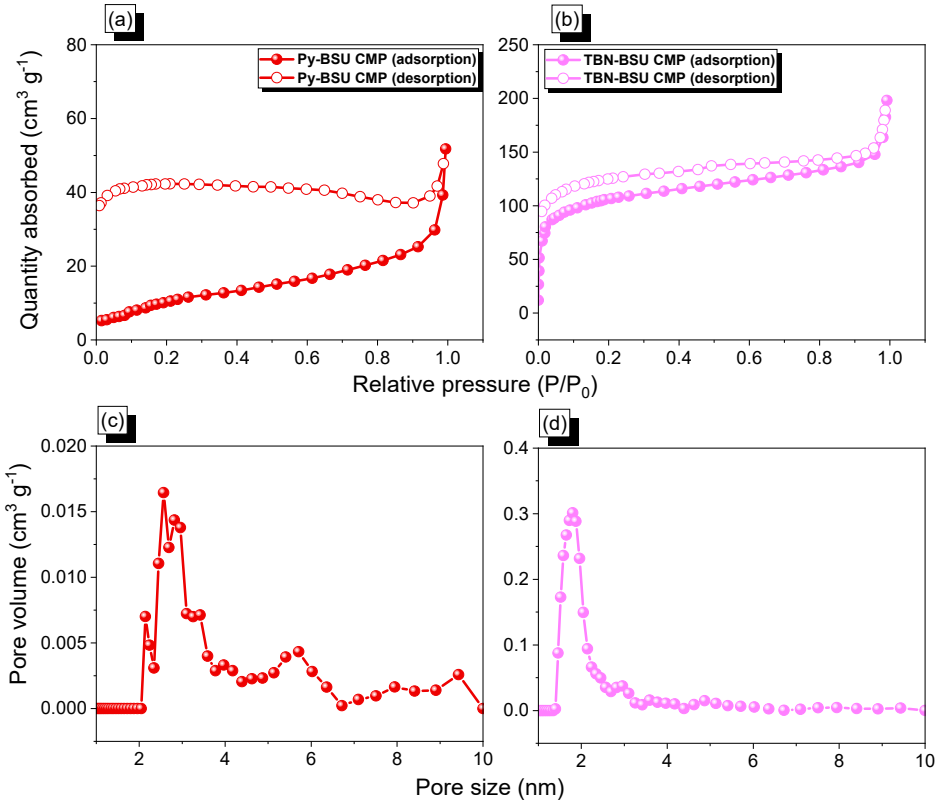

Figure 2. (**a**,**b**) N_2 adsorption/desorption isotherms and (**c**,**d**) pore size distribution profiles of (**a**,**c**) Py-BSU CMP and (**b**,**d**) TBN-BSU CMP.

The spatial ordering of Py-BSU CMP and TBN-BSU CMP was determined by X-ray diffraction analysis in the angular (2θ) range of 5–50°. Crystalline peaks were not observed in the XRD results, and the broad peaks in Figure S29 show the amorphous features of Py-BSU CMP and TBN-BSU CMP. The powder morphologies by SEM images of Py-BSU CMP and TBN-BSU CMP are shown in Figure 3a,b, respectively. The former nanosheets agglomerated slightly; the latter cluster phenomenon occurs because of the extremely small size of spherical nanoparticles. Furthermore, the presence of carbon (C), oxygen (O), and sulfur (S) atoms in both Py-BSU CMP and TBN-BSU CMP were confirmed through EDS-SEM mapping (Figure 3c–i). The weight contents of C, O, and S in Py-BSU CMP were 78.80, 16.82, and 4.38%, respectively (Figure S30a). In TBN-BSU CMP, the weight contents were 70.9, 26.64, and 2.46% for C, O, and S atoms, respectively (Figure S30b). The TEM images (Figure S31) of both Py-BSU CMP and TBN-BSU CMP show that the structure was amorphous and that nanometer-scale holes were distributed uniformly.

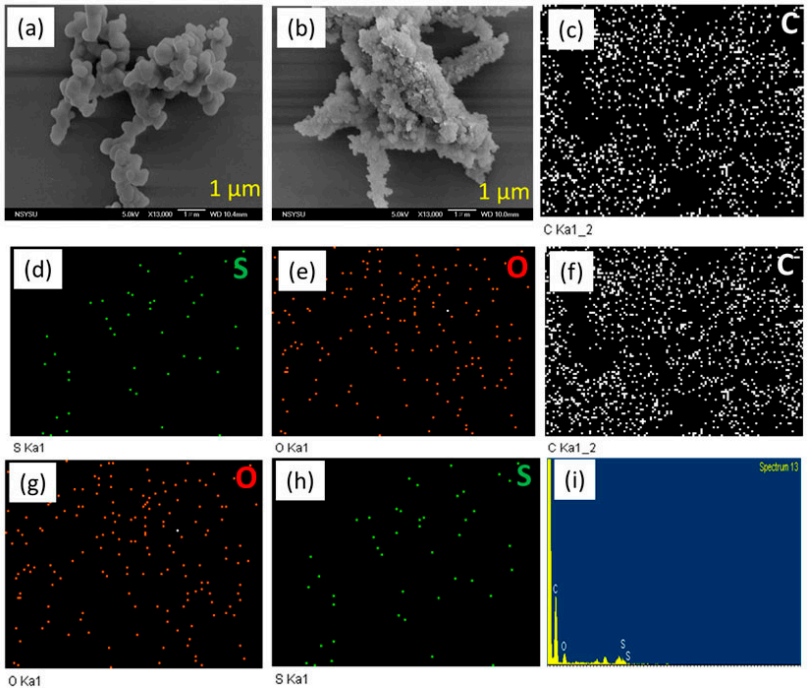

Figure 3. SEM images (**a**,**b**) and EDS-SEM mapping (**c**–**i**) of Py-BSU CMP (**a**,**c**–**e**) and TBN-BSU CMP (**b**,**f**–**i**).

The CO_2 capacities of TBN-BSU CMP and Py-BSU CMP were 1.6 and 1.45 mmol g^{-1}, respectively, as displayed in Figure 4. The excellent performance of TBN-BSU CMP for CO_2 uptake is due to its high pore volume, BET surface area, and tunable pore size.

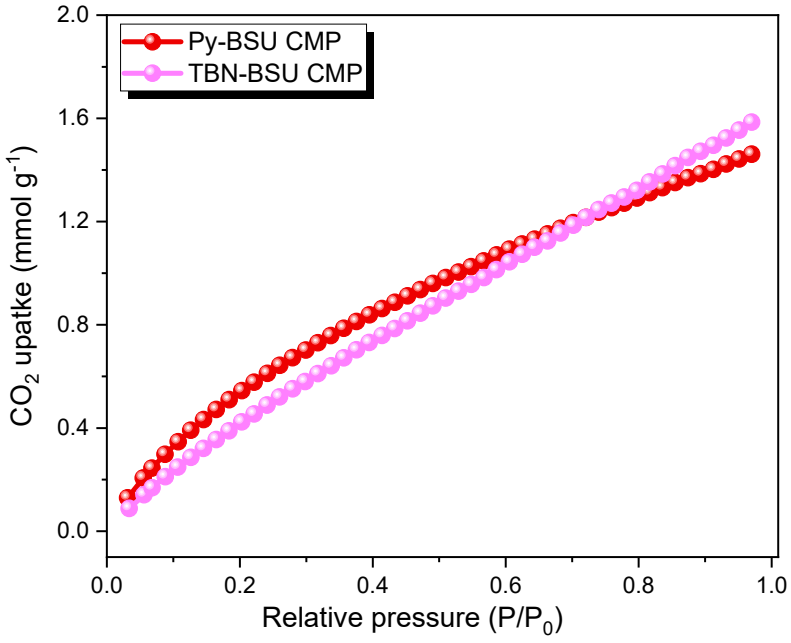

Figure 4. CO_2 uptake of Py-BSU CMP and TBN-BSU CMP was recorded at 298 K.

2.2. Electrochemical Measurements of Py-BSU CMP and TBN-BSU CMP

We used 1 M KOH aqueous solution as the electrolyte in a three-electrode system and compared the electrochemical performance of Py-BSU CMP and TBN-BSU CMP by cyclic voltammetry (CV) and galvanostatic charge–discharge (GCD). The working electrode, counter electrode, and reference electrode of the three-electrode system are composed of

glassy carbon, platinum, and Hg/HgO, respectively. The CV curves of Py-BSU CMP and TBN-BSU CMP at scan rates from 5 to 200 mV s^{-1} are shown in Figure 5a,b, and the overall leaf-like shape suggests a response originating from the electric double-layer capacitance (EDLC). Among them, as the scan rate increased from 5 to 200 mV s^{-1}, the maintained shape of the CV curves indicates the excellent rate capability of the material. Figure 5c,d report the GCD curves detected at current densities ranging from 0.5 to 20 A g^{-1}. Slightly curved triangles are characteristic of EDLC.

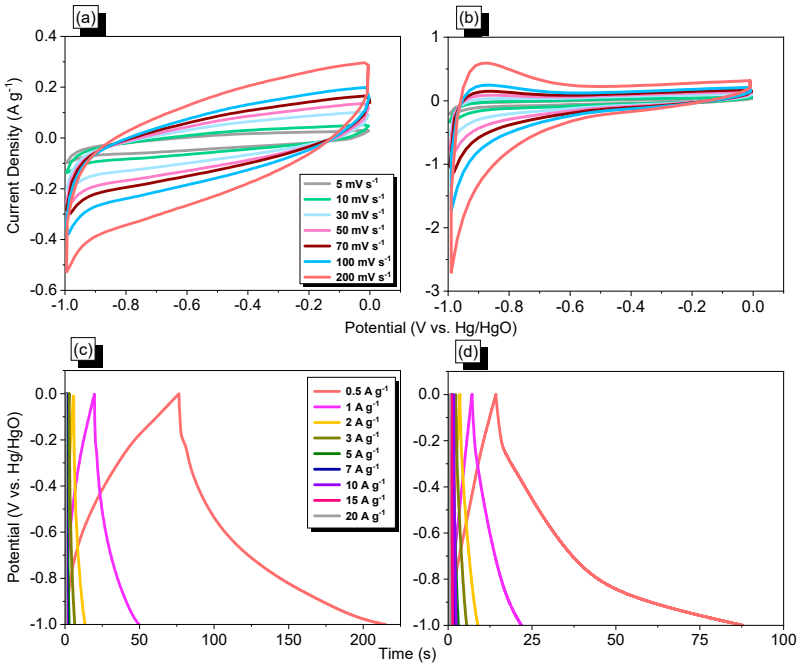

Figure 5. CV (**a**,**b**) and GCD (**c**,**d**) curves of TBN-BSU CMP (**a**,**c**) and Py-BSU CMP (**b**,**d**).

As shown in Figure 6a, at a current density of 0.5 A g^{-1}, the specific capacitance values of Py-BSU CMP and TBN-BSU CMP calculated by GCD curves were 38 and 70 F g^{-1}. In contrast, TBN-BSU CMP exhibited superior electrochemical behavior due to the more extended conjugated structure of the TBN unit and high surface area. The improvement of the π system increased the charge transfer efficiency in contact with the electrolyte and further promoted the performance of the supercapacitor through this process. From another point of view, the capacitance value shrunk when the current density increased from 0.5 to 20 A g^{-1}. This can be attributed to the diffusion problem caused by electrolyte ions not fully permeating into the electrode material due to insufficient time in the high current environment. Figure 6b,c demonstrate the measured stability over 2000 cycles at a current density of 10 A g^{-1}. The capacitance retention rates of Py-BSU CMP and TBN-BSU CMP were 99.8% and 99.9%, respectively. The extremely small capacitance decay indicates that the material has excellent electrochemical reversibility. Figure 6d shows that the specific capacitance value of TBN-BSU CMP precursor (70 F g^{-1}) is higher than CoPc-CMP (13.8 F g^{-1}) [78], H-THAQ (15 F g^{-1}) [79], TBN-TPE-CMP (18.45 F g^{-1}) [32], TBN-Py-CMP (31 F g^{-1}) [32], POSS-F-POIP (36.2 F g^{-1}) [31], Py-BSU CMP (38 F g^{-1}), pyrolysis nutshell (45 F g^{-1}) [80], COFs (48 F g^{-1}) [81], HPCs (48 F g^{-1}) [82], TBN-BSU CMP (70 F g^{-1}), and other candidate materials.

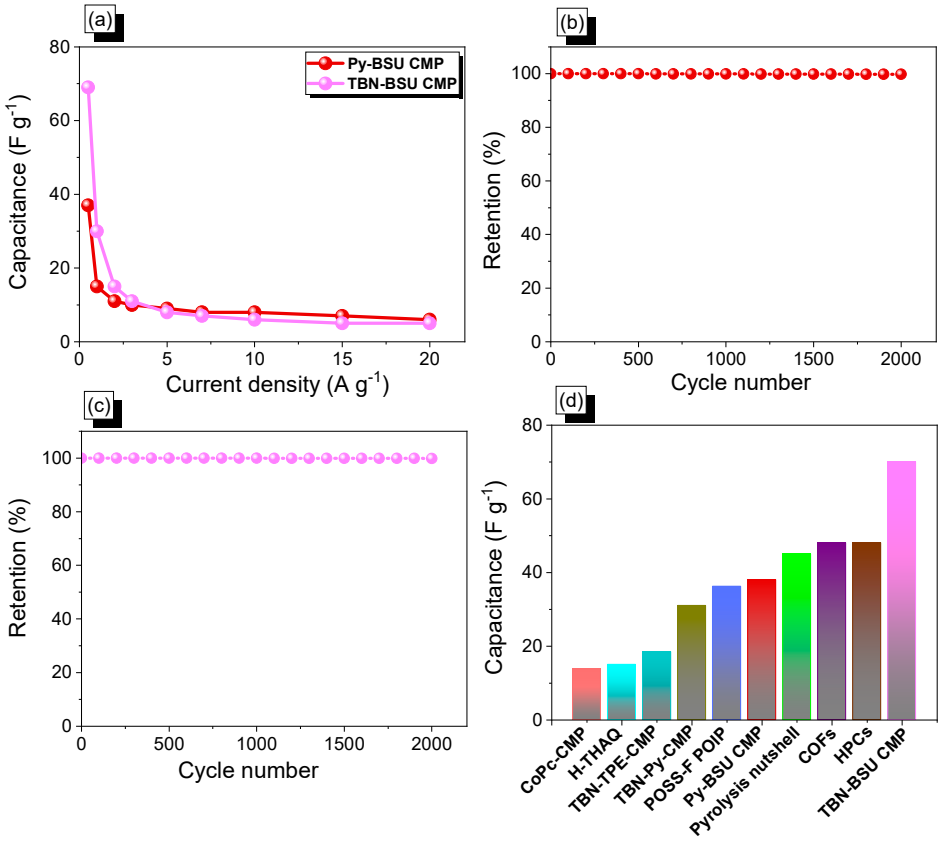

Figure 6. Capacitance (**a**) and stability (**b**,**c**) and the performance of Py-BSU CMP and TBN-BSU CMP precursors compared with other POPs in energy storage (**d**).

In Figures 7 and S32, the EIS results indicated that Py-BSU CMP and TBN-BSU CMP have slightly different Nyquist curves, suggesting they have different resistances. In detail, TBN and Py-BSU CMP showed a specific resistance of 9 and 23 ohm, respectively. The charge transfer rate studies were tested through EIS within the frequency range of 100 mHz to 100 kHz at the open circuit potential and 5 mV as an amplitude. It should be noticed that a smaller semi-circuit was observed for TBN-BSU CMP with lower resistance than Py-BSU CMP, indicating a lower resistance and lower charge transfer resistance. The results were fitted to a simulation circuit composed of four elements of the series resistance (R_s), the charge-transfer resistance (R_{ct}), the electrical double-layer capacitance (C_{dl}), and the Warburg diffusion impedance (W_d), as displayed in the inset of the figure of Randles Cell. It is important to notice that low-resistance materials can improve energy storage because they have fast charge transport capabilities. Therefore, TBN-BSU CMP is a better choice for energy storage applications. Due to its high surface area, structural integrity, and compatibility with bis-sulfone units, TBN-BSU CMP exhibited this behavior [83–88].

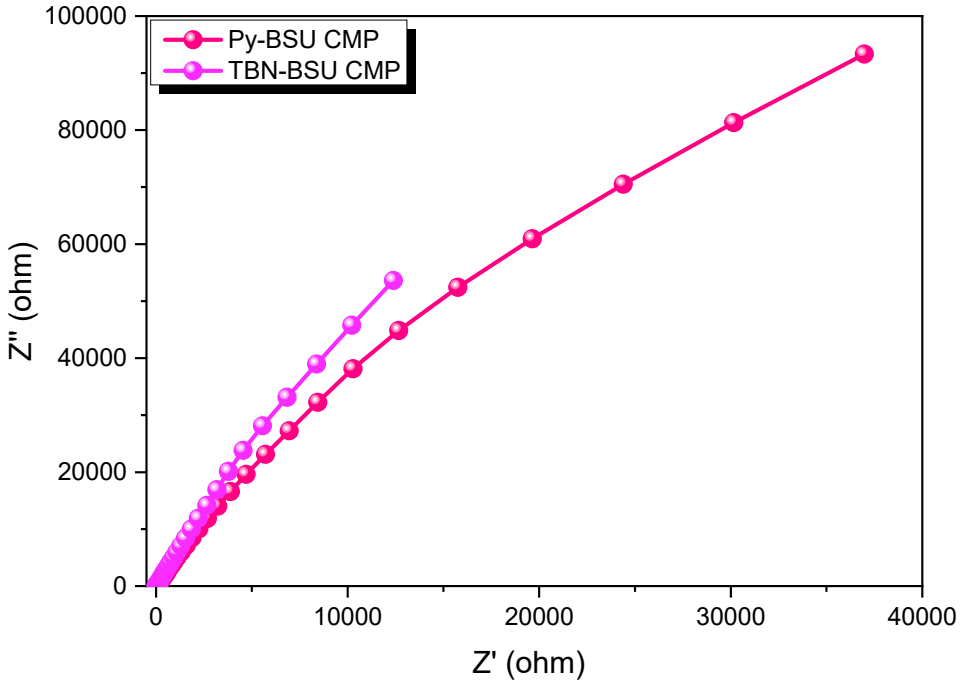

Figure 7. Electrochemical impedance spectroscopy (EIS) of Py-BSU CMP and TBN-BSU CMP electrode materials, recorded at 0.5 Hz.

3. Materials and Methods

3.1. Materials

Anhydrous magnesium sulfate ($MgSO_4$, 99.5%), pyrene (Py), benzophenone (99%), $PdCl_2(PPh_3)_2$, bromine solution (Br_2), copper(I) iodide (CuI, 99%), dichloromethane (DCM), glacial acetic acid (AcOH), hydrogen peroxide (H_2O_2), potassium carbonate (K_2CO_3, 99.9%), $Pd(PPh_3)_4$, thianthrene (THT, 99%), titanium tetrachloride ($TiCl_4$, 99.9%), trimethylsilylacetylene (TMSA, 98%), triphenylphosine (PPh_3, 99%), zinc powder (Zn, 98%) were purchased from Sigma-Aldrich (Gillingham, UK) and Acros Organics (Geel, Belgium).

3.2. Synthesis of 2,8-Dibromothianthrene (THT-Br_2)

Br_2 solution (6 mL, 0.116 mol) was added dropwise to thianthrene (3.24 g, 0.015 mol) dissolved in AcOH (60 mL). The reactant was heated to 90 °C and agitated for one day. Distilled water (30 mL) was then added to the mixture once it had cooled to room temperature. The resultant precipitate was filtered out and properly washed with a 5% $NaHCO_3$ solution and water. The further purification by recrystallization from MeOH/DCM afforded THT-Br_2 a white solid (Scheme S1). FTIR (Figure S1): 3066 cm^{-1}. ^{1}H NMR (Figure S2): 7.71, 7.62, 7.31 ppm. ^{13}C NMR (Figure S3): 138.00–122.44 ppm.

3.3. Synthesis of 2,8-Dibromothianthrene-5,5′,10,10′-Tetraoxide (BSU-Br_2)

H_2O_2 (70 mL, 2.984 mol) was added dropwise to THT-Br_2 (2.55 g, 0.007 mol), dissolved in glacial acetic acid (55 mL). The reactant was heated to 90 °C and stirred for 1 day. After cooling to room temperature, the resulting precipitate was filtered off and washed thoroughly with 5% $NaHCO_3$ solution and H_2O. Finally, the BSU-Br_2 product was purified by recrystallization from MeOH/DCM mixture affording BSU-Br_2 a white solid (Scheme S2). FTIR (Figure S4): 3068 and 1171(SO_2 group) cm^{-1}. ^{1}H NMR (Figure S5): 8.38–7.52 ppm (aromatic protons). ^{13}C NMR (Figure S6): 137.54–124.62 ppm.

3.4. Synthesis of 1,3,6,8-Tetrabromopyrene (Py-Br_4)

Br_2 (3.5 mL, 0.068 mol) was injected dropwise into a Py monomer (3.00 g, 0.015 mol) dissolved in nitrobenzene (30 mL). The reaction mixture was then heated to 120 °C and

stirred for 24 h. After filtration through EtOH, the green solid was collected and dried at 60 °C (Scheme S3). FTIR (Figure S7): 3053 and 682 (C-Br group) cm^{-1}.

3.5. Synthesis of 1,3,6,8-Tetrakis(trimethylsilanylethynyl)pyrene (Py-TMS)

Py-Br_4 (1.00 g, 1.924 mmol), $Pd(PPh_3)_4$ (0.13 g, 0.112 mmol), PPh_3 (0.11 g, 0.419 mmol), and CuI (0.06 g, 0.315 mmol) were dissolved in Et_3N (28 mL) and anhydrous toluene (28 mL). TMSA (1.52 g, 15.48 mmol) was added dropwise to the reactant after heating to 50 °C. The mixture was then heated to 80 °C for two days. The solvent was removed via a rotary evaporator, and the orange solid dried under vacuum at 60 °C (Scheme S3). FTIR (KBr, Figure S8): 2908 (aliphatic C-H stretching), 2100 (C≡C stretching). ^{1}H NMR (Figure S9): 8.57-8.30 (aromatic), 0.413 (36H). ^{13}C NMR (Figure S10): 135.70–101.60.

3.6. Synthesis of 1,3,6,8-Tetraethynylpyrene (Py-T)

K_2CO_3 (5.70 g, 41.2 mmol) and Py-TMS (2.00 g, 3.395 mmol) were dissolved in anhydrous MeOH (50 mL). The mixture was stirred for two days at room temperature. Filtering and drying the solid at 60 °C were done to afford a brown solid (Scheme S3). FTIR (Figure S11): 3279 (≡C–H), 2186 (C≡C). ^{1}H NMR (Figure S12): 8.68–8.38 (aromatic), 3.67 (s, 4H). ^{13}C NMR (Figure S13): 133.80–82.00 ppm.

3.7. Synthesis of Tetraphenylethylene (TPE), 1,1,2,2-Tetrakis(4-bromophenyl)ethene (TPE-Br_4) and 2,7,10,15-Tetrabromodibenzo[g,p]chrysene (TBN-Br_4)

The synthesis detail for TPE, TPE-Br_4, and TBN-Br_4 are provided in the supporting information file, and their FTIR and NMR data confirmed their chemical structure (Schemes S4 and S5, Figures S14–S22).

3.8. Synthesis of 2,7,10,15-Tetrakis(trimethylsilyl)ethynyl)dibenzo[g,p]chrysene (TBN-TMS)

In 125 mL of diethylamine, 1.5 g of TBN-Br_4 (2.33 mmol) was dissolved. Then the solution was treated with a combination of CuI (0.11 g), $PdCl_2(PPh_3)_2$ (0.08 g), and ethynyltrimethylsilane (1.83 g, 18.63 mmol). After 24 h of stirring at 80 °C, the solvent was removed under reduced pressure, and the product was then purified using flash chromatography on a silica gel column with DCM as an eluent to produce a yellow solid (Scheme S6, 1.3 g, 86%). FTIR (Figure S23): 3291 (C≡C-H), 3031 (aromatic C-H), 2957 (aliphatic C-H), 2156 (C≡C), 1632 (C=C). ^{1}H NMR (Figure S24): δ 8.77, 8.47, 7.69, 0.34 (s, 36H, CH_3). ^{13}C NMR (Figure S25): 131.24, 128.74, 121.90, 105.38, 96.34, 30.59, 3.50.

3.9. Synthesis of 2,7,10,15-Tetraethynyldibenzo[g,p]chrysene (TBN-T)

The TBN-TMS (1 g, 1.40 mmol) was dissolved in 60 mL of MeOH and 40 mL of DCM before being mixed for 24 h with 1.2 g of K_2CO_3 (8.65 mmol). Following this, the solvent was removed using a vacuum. The resulting solid was dissolved with 50 mL of DCM and then extracted with H_2O to afford TBN-T (0.8 g, 80%) as an orange solid after the solvent was removed under vacuum (Scheme S7). FTIR (KBr, cm^{-1}, Figure S26): 3291 (C≡C-H), 3057 (aromatic C-H), 2106 (C≡C), 1604 (C=C). ^{1}H NMR (Figure S27): 8.81 (s, 4H), 8.53 (s, 4H), 7.73 (s, 4H), 3.30 (s, 4H). ^{3}C NMR (Figure S28): 135.70, 132.40, 127.80, 119.20, 103.50, 101.60, 84.21, 78.87.

3.10. Synthesis of Py-BSU CMP

BSU-Br_2 (0.293 g, 0.669 mmol), Py-T (0.1 g, 0.333 mmol), $Pd(PPh_3)_4$ (0.038 g, 0.033 mmol), PPh_3 (0.0087 g, 0.033 mmol), and CuI (0.0063 g, 0.033 mmol) were added to Et_3N (7 mL) and DMF (7 mL) and heated to 90 °C for 3 days. The filtered powder was washed stepwise with THF, MeOH, and acetone. The solid was dried under vacuum at 110 °C overnight to obtain a dark red powder (Scheme 1a).

3.11. Synthesis of TBN-BSU CMP

$BSU\text{-}Br_2$ (0.206 g, 0.470 mmol), TBN-T (0.1 g, 0.236 mmol), $Pd(PPh_3)_4$ (0.027 g, 0.023 mmol), PPh_3 (0.006 g, 0.023 mmol), and CuI (0.006 g, 0.032 mmol) was added in Et_3N (5 mL) and DMF (5 mL) and heated to 90 °C for 3 days. The filtered powder was washed well step by step with THF, MeOH, and acetone. Dried the solid under vacuum at 110 °C overnight and then gained a yellow powder (Scheme 1b).

4. Conclusions

In this study, we successfully synthesized two conjugated microporous polymers, Py-BSU CMP and TBN-BSU CMP, using Sonogashira-Hagihara cross-coupling of $BSU\text{-}Br_2$ with Py-T and TBN-T, respectively. We characterized the chemical structures, physical properties, porosity, and morphology of these CMPs using various analytical techniques, including FTIR, solid-state ^{13}C NMR spectroscopy, BET, SEM, and TEM. Both Py-BSU CMP and TBN-BSU CMP showed excellent thermal stability with T_{d10} up to 383 °C and char yield up to 48 wt% at 800 °C as measured by TGA. We also investigated the electrochemical performance of these CMPs and found that TBN-BSU CMP exhibited better performance due to its more extended π-conjugated system, higher specific surface area (391 $m^2\ g^{-1}$), and total pore volume (0.30 $cm^3\ g^{-1}$). Under the three-electrode measurement system, TBN-BSU CMP showed significantly better electrochemical performance with a capacitance of 70 F g^{-1} at a current density of 0.5 A g^{-1} compared to Py-BSU CMP. TBN-BSU CMP also demonstrated excellent stability with less capacitance decay (99.9%) in long-life-cycle energy storage devices. Finally, we believe that these BSU-linked CMPs, Py-BSU and TBN-BSU CMPs, hold great potential for other applications such as H_2 production and gas conversion. Overall, our findings suggest that these CMPs could be attractive candidates for various energy storage and conversion applications.

Supplementary Materials: The following supporting information can be downloaded at: https://www.mdpi.com/article/10.3390/molecules28073234/s1, Scheme S1: Synthesis of $THT\text{-}Br_2$; Scheme S2: Synthesis of $BSU\text{-}Br_2$; Scheme S3: Synthesis of Py-T; Scheme S4: Synthesis of TPE and $TPE\text{-}Br_4$; Scheme S5: Synthesis of $TBN\text{-}Br_4$; Scheme S6: Synthesis of TBN-TMS; Scheme S7: Synthesis of TBN-T; Figure S1: FTIR profile of $THT\text{-}Br_2$; Figure S2: ^1H-NMR spectrum of $THT\text{-}Br_2$ in $CDCl_3$; Figure S3: ^{13}C-NMR spectrum of $THT\text{-}Br_2$ in $CDCl_3$; Figure S4: FTIR profile of $BSU\text{-}Br_2$; Figure S5: ^1H-NMR spectrum of $BSU\text{-}Br_2$; Figure S6: ^{13}C-NMR spectrum of $BSU\text{-}Br_2$; Figure S7: FT-IR spectrum of $Py\text{-}Br_4$; Figure S8: FT-IR spectrum of Py-TMS; Figure S9: ^1H NMR spectrum of Py-TMS; Figure S10: ^{13}C NMR spectrum of Py-TMS; Figure S11: FT-IR spectrum of Py-T; Figure S12: ^1H NMR spectrum of Py-T; Figure S13: ^{13}C NMR spectrum of Py-T; Figure S14: FT-IR spectrum of TPE; Figure S15: ^1H NMR spectrum of TPE; Figure S16: ^{13}C NMR spectrum of TPE; Figure S17: FT-IR spectrum of $TPE\text{-}Br_4$; Figure S18: ^1H NMR spectrum of $TPE\text{-}Br_4$; Figure S19: ^{13}C NMR spectrum of $TPE\text{-}Br_4$; Figure S20: FTIR spectrum of $TBN\text{-}Br_4$; Figure S21: ^1H-NMR spectrum of $TBN\text{-}Br_4$. Figure S22. ^{13}C-NMR spectrum of $TBN\text{-}Br_4$. Figure S23. FTIR spectrum of TBN-TMS; Figure S24: ^1H NMR spectrum of TBN-TMS; Figure S25: ^{13}C NMR spectrum of TBN-TMS; Figure S26: FTIR spectrum of TBN-T; Figure S27: ^1H NMR spectrum of TBN-T; Figure S28: ^{13}C NMR spectrum of TBN-T; Figure S29: XRD profiles of Py-BSU CMP and TBN-BSU CMP; Figure S30: Weight elements contents profiles of (a) Py-BSU CMP and (b) TBN-BSU CMP; Figure S31: TEM images of Py-BSU CMP and TBN-BSU CMP; Figure S32: Fitted circuits of the Nyquist plots of Py-BSU CMP and TBN-BSU CMP.

Author Contributions: Conceptualization, M.G.M. and S.-Y.C.; methodology, M.G.M., S.-Y.C., M.E., M.M.S., A.O.M. and S.-W.K.; validation, M.G.M., S.-Y.C., M.E., M.M.S., A.O.M. and S.-W.K.; formal analysis, M.G.M., S.-Y.C., M.E., M.M.S., A.O.M. and S.-W.K.; investigation, M.G.M., S.-Y.C., M.E., M.M.S., A.O.M. and S.-W.K.; data curation, M.G.M.; writing—original draft preparation, M.G.M. and S.-W.K.; writing—review and editing, M.G.M. and S.-W.K.; visualization, M.G.M. and S.-W.K.; supervision, M.G.M. and S.-W.K.; project administration, S.-W.K.; funding acquisition, S.-W.K. All authors have read and agreed to the published version of the manuscript.

Funding: This study was supported financially by the Ministry of Science and Technology, Taiwan, under contracts NSTC 110-2124-M-002-013 and 111-2223-E-110-004.

Institutional Review Board Statement: Not applicable.

Informed Consent Statement: Not applicable.

Data Availability Statement: The data presented in this study are available on request from the corresponding author.

Acknowledgments: The authors thank National Sun Yat-sen University staff for their assistance with the TEM (ID: EM022600) experiments.

Conflicts of Interest: The authors declare no conflict of interest.

References

1. Loganathan, N.N.; Perumal, V.; Pandian, B.R.; Atchudan, R.; Edison, T.N.J.I.; Ovinis, M. Recent studies on polymeric materials for supercapacitor development. *J. Energy Storage* **2022**, *49*, 104149. [CrossRef]
2. Zhao, D.; Wang, H.; Bai, Y.; Yang, H.; Song, H.; Li, B. Preparation of Advanced Multi-Porous Carbon Nanofibers for High-Performance Capacitive Electrodes in Supercapacitors. *Polymers* **2022**, *15*, 213. [CrossRef]
3. Mohamed, M.G.; Mansoure, T.H.; Samy, M.M.; Takashi, Y.; Mohammed, A.A.K.; Ahamad, T.; Alshehri, S.M.; Kim, J.; Matsagar, B.M.; Wu, K.C.-W.; et al. Ultrastable Conjugated Microporous Polymers Containing Benzobisthiadiazole and Pyrene Building Blocks for Energy Storage Applications. *Molecules* **2022**, *27*, 2025. [CrossRef]
4. Samy, M.M.; Mohamed, M.G.; Kuo, S.-W. Conjugated Microporous Polymers Based on Ferrocene Units as Highly Efficient Electrodes for Energy Storage. *Polymers* **2023**, *15*, 1095. [CrossRef]
5. Wang, H.; Yao, L.; Zuo, H.; Ruan, F.; Wang, H. Fabrication of Porous Carbon Nanofibers from Polymer Blends Using Template Method for Electrode-Active Materials in Supercapacitor. *Molecules* **2023**, *28*, 2228. [CrossRef]
6. Bai, Y.; Liu, C.; Chen, T.; Li, W.; Zheng, S.; Pi, Y.; Luo, Y.; Pang, H. MXene-copper/cobalt hybrids via lewis acidic molten salts etching for high performance symmetric supercapacitors. *Angew. Chem.* **2021**, *133*, 25522–25526. [CrossRef]
7. Reece, R.; Lekakou, C.; Smith, P.A. A high-performance structural supercapacitor. *ACS Appl. Mater. Interfaces* **2020**, *12*, 25683–25692. [CrossRef]
8. Şahin, M.E.; Blaabjerg, F.; Sangwongwanich, A. A comprehensive review on supercapacitor applications and developments. *Energies* **2022**, *15*, 674. [CrossRef]
9. Sahoo, S.; Kumar, R.; Joanni, E.; Singh, R.K.; Shim, J.-J. Advances in pseudocapacitive and battery-like electrode materials for high performance supercapacitors. *J. Mater. Chem. A* **2022**, *10*, 13190–13240. [CrossRef]
10. Mohamed, M.G.; Elsayed, M.H.; Ye, Y.; Samy, M.M.; Hassan, A.E.; Mansoure, T.H.; Wen, Z.; Chou, H.-H.; Chen, K.-H.; Kuo, S.-W. Construction of Porous Organic/Inorganic Hybrid Polymers Based on Polyhedral Oligomeric Silsesquioxane for Energy Storage and Hydrogen Production from Water. *Polymers* **2023**, *15*, 182. [CrossRef] [PubMed]
11. Septiani, N.L.W.; Kaneti, Y.V.; Fathoni, K.B.; Wang, J.; Ide, Y.; Yuliarto, B.; Dipojono, H.K.; Nanjundan, A.K.; Golberg, D.; Bando, Y. Self-assembly of nickel phosphate-based nanotubes into two-dimensional crumpled sheet-like architectures for high-performance asymmetric supercapacitors. *Nano Energy* **2020**, *67*, 104270. [CrossRef]
12. Samy, M.M.; Mohamed, M.G.; Sharma, S.U.; Chaganti, S.V.; Mansoure, T.H.; Lee, J.-T.; Chen, T.; Kuo, S.-W. Constructing conjugated microporous polymers containing triphenylamine moieties for high-performance capacitive energy storage. *Polymer* **2023**, *264*, 125541. [CrossRef]
13. Shi, R.; Han, C.; Duan, H.; Xu, L.; Zhou, D.; Li, H.; Li, J.; Kang, F.; Li, B.; Wang, G. Redox-active organic sodium anthraquinone-2-sulfonate (AQS) anchored on reduced graphene oxide for high-performance supercapacitors. *Adv. Energy Mater.* **2018**, *8*, 1802088. [CrossRef]
14. Mohamed, M.G.; Chaganti, S.V.; Li, M.-S.; Samy, M.M.; Sharma, S.U.; Lee, J.-T.; Elsayed, M.H.; Chou, H.-H.; Kuo, S.-W. Ultrastable Porous Organic Polymers Containing Thianthrene and Pyrene Units as Organic Electrode Materials for Supercapacitors. *ACS Appl. Energy Mater.* **2022**, *5*, 6442–6452. [CrossRef]
15. Mohamed, M.G.; Sharma, S.U.; Liu, N.-Y.; Mansoure, T.H.; Samy, M.M.; Chaganti, S.V.; Chang, Y.-L.; Lee, J.-T.; Kuo, S.-W. Ultrastable covalent triazine organic framework based on anthracene moiety as platform for high-performance carbon dioxide adsorption and supercapacitors. *Int. J. Mol. Sci.* **2022**, *23*, 3174. [CrossRef] [PubMed]
16. Harjanne, A.; Korhonen, J.M. Abandoning the concept of renewable energy. *Energy Policy* **2019**, *127*, 330–340. [CrossRef]
17. Lund, H. Renewable energy strategies for sustainable development. *Energy* **2007**, *32*, 912–919. [CrossRef]
18. Moriarty, P.; Honnery, D. What is the global potential for renewable energy? *Renew. Sustain. Energy Rev.* **2012**, *16*, 244–252. [CrossRef]
19. Chu, S.; Majumdar, A. Opportunities and challenges for a sustainable energy future. *Nature* **2012**, *488*, 294–303. [CrossRef]
20. Chung, W.-T.; Mekhemer, I.M.A.; Mohamed, M.G.; Elewa, A.M.; EL-Mahdy, A.F.M.; Chou, H.-H.; Kuo, S.-W.; Wu, K.C.-W. Recent advances in metal/covalent organic frameworks based materials: Their synthesis, structure design and potential applications for hydrogen production. *Coord. Chem. Rev.* **2023**, *483*, 215066. [CrossRef]
21. Omer, A.M. Energy, environment and sustainable development. *Renew. Sustain. Energy Rev.* **2008**, *12*, 2265–2300. [CrossRef]
22. Wang, D.-G.; Liang, Z.; Gao, S.; Qu, C.; Zou, R. Metal-organic framework-based materials for hybrid supercapacitor application. *Coord. Chem. Rev.* **2020**, *404*, 213093. [CrossRef]

23. Dai, Y.; Li, W.; Chen, Z.; Zhu, X.; Liu, J.; Zhao, R.; Wright, D.S.; Noori, A.; Mousavi, M.F.; Zhang, C. An air-stable electrochromic conjugated microporous polymer as an emerging electrode material for hybrid energy storage systems. *J. Mater. Chem. A.* **2019**, *7*, 16397–16405. [CrossRef]
24. Mohamed, M.G.; Tsai, M.-Y.; Wang, C.-F.; Huang, C.-F.; Danko, M.; Dai, L.; Chen, T.; Kuo, S.-W. Multifunctional polyhedral oligomeric silsesquioxane (POSS) based hybrid porous materials for CO_2 uptake and iodine adsorption. *Polymers* **2021**, *13*, 221. [CrossRef] [PubMed]
25. Samy, M.M.; Mekhemer, I.M.; Mohamed, M.G.; Elsayed, M.H.; Lin, K.-H.; Chen, Y.-K.; Wu, T.-L.; Chou, H.-H.; Kuo, S.-W. Conjugated microporous polymers incorporating Thiazolo [5,4-d] thiazole moieties for Sunlight-Driven hydrogen production from water. *Chem. Eng. J.* **2022**, *446*, 137158. [CrossRef]
26. Mohamed, M.G.; Samy, M.M.; Mansoure, T.H.; Sharma, S.U.; Tsai, M.-S.; Chen, J.-H.; Lee, J.-T.; Kuo, S.-W. Dispersions of 1,3,4-oxadiazole-linked conjugated microporous polymers with carbon nanotubes as a high-performance electrode for supercapacitors. *ACS Appl. Energy Mater.* **2022**, *5*, 3677–3688. [CrossRef]
27. Samy, M.M.; Mohamed, M.G.; Mansoure, T.H.; Meng, T.S.; Khan, M.A.R.; Liaw, C.-C.; Kuo, S.-W. Solid state chemical transformations through ring-opening polymerization of ferrocene-based conjugated microporous polymers in host–guest complexes with benzoxazine-linked cyclodextrin. *J. Taiwan Inst. Chem. Eng.* **2022**, *132*, 104110. [CrossRef]
28. Weng, T.-H.; Mohamed, M.G.; Sharma, S.U.; Chaganti, S.V.; Samy, M.M.; Lee, J.-T.; Kuo, S.-W. Ultrastable three-dimensional triptycene-and tetraphenylethene-conjugated microporous polymers for energy storage. *ACS Appl. Energy Mater.* **2022**, *5*, 14239–14249. [CrossRef]
29. Ejaz, M.; Samy, M.M.; Ye, Y.; Kuo, S.-W.; Gamal Mohamed, M. Design Hybrid Porous Organic/Inorganic Polymers Containing Polyhedral Oligomeric Silsesquioxane/Pyrene/Anthracene Moieties as a High-Performance Electrode for Supercapacitor. *Int. J. Mol. Sci.* **2023**, *24*, 2501. [CrossRef]
30. Sheberla, D.; Bachman, J.C.; Elias, J.S.; Sun, C.-J.; Shao-Horn, Y.; Dincă, M. Conductive MOF electrodes for stable supercapacitors with high areal capacitance. *Nat. Mater.* **2017**, *16*, 220–224. [CrossRef]
31. Mohamed, M.G.; Mansoure, T.H.; Takashi, Y.; Samy, M.M.; Chen, T.; Kuo, S.-W. Ultrastable porous organic/inorganic polymers based on polyhedral oligomeric silsesquioxane (POSS) hybrids exhibiting high performance for thermal property and energy storage. *Microporous Mesoporous Mater.* **2021**, *328*, 111505. [CrossRef]
32. Samy, M.M.; Mohamed, M.G.; El-Mahdy, A.F.; Mansoure, T.H.; Wu, K.C.-W.; Kuo, S.-W. High-performance supercapacitor electrodes prepared from dispersions of tetrabenzonaphthalene-based conjugated microporous polymers and carbon nanotubes. *ACS Appl. Mater. Interfaces* **2021**, *13*, 51906–51916. [CrossRef]
33. Shown, I.; Ganguly, A.; Chen, L.C.; Chen, K.H. Conducting polymer-based flexible supercapacitor. *Energy Sci. Eng.* **2015**, *3*, 2–26. [CrossRef]
34. Karthikeyan, S.; Narenthiran, B.; Sivanantham, A.; Bhatlu, L.D.; Maridurai, T. Supercapacitor: Evolution and review. *Mater. Today Proc.* **2021**, *46*, 3984–3988. [CrossRef]
35. Wang, Y.; Zhang, L.; Hou, H.; Xu, W.; Duan, G.; He, S.; Liu, K.; Jiang, S. Recent progress in carbon-based materials for supercapacitor electrodes: A review. *J. Mater. Sci.* **2021**, *56*, 173–200. [CrossRef]
36. Borchardt, L.; Oschatz, M.; Kaskel, S. Tailoring porosity in carbon materials for supercapacitor applications. *Mater. Horiz.* **2014**, *1*, 157–168. [CrossRef]
37. Sharma, K.; Arora, A.; Tripathi, S.K. Review of supercapacitors: Materials and devices. *J. Energy Storage* **2019**, *21*, 801–825.
38. Raza, W.; Ali, F.; Raza, N.; Luo, Y.; Kim, K.-H.; Yang, J.; Kumar, S.; Mehmood, A.; Kwon, E.E. Recent advancements in supercapacitor technology. *Nano Energy* **2018**, *52*, 441–473. [CrossRef]
39. Cherusseri, J.; Choudhary, N.; Kumar, K.S.; Jung, Y.; Thomas, J. Recent trends in transition metal dichalcogenide based supercapacitor electrodes. *Nanoscale Horiz.* **2019**, *4*, 840–858. [CrossRef]
40. Kouchachvili, L.; Yaïci, W.; Entchev, E. Hybrid battery/supercapacitor energy storage system for the electric vehicles. *J. Power Sources* **2018**, *374*, 237–248. [CrossRef]
41. Salunkhe, R.R.; Kaneti, Y.V.; Yamauchi, Y. Metal–organic framework-derived nanoporous metal oxides toward supercapacitor applications: Progress and prospects. *ACS Nano* **2017**, *11*, 5293–5308. [CrossRef] [PubMed]
42. Chen, G.Z. Supercapacitor and supercapattery as emerging electrochemical energy stores. *Int. Mater. Rev.* **2017**, *62*, 173–202. [CrossRef]
43. Dyatkin, B.; Presser, V.; Heon, M.; Lukatskaya, M.R.; Beidaghi, M.; Gogotsi, Y. Development of a green supercapacitor composed entirely of environmentally friendly materials. *ChemSusChem* **2013**, *6*, 2269–2280. [CrossRef]
44. Kang, J.; Wen, J.; Jayaram, S.H.; Yu, A.; Wang, X. Development of an equivalent circuit model for electrochemical double layer capacitors (EDLCs) with distinct electrolytes. *Electrochim. Acta.* **2014**, *115*, 587–598. [CrossRef]
45. Xu, B.; Wu, F.; Chen, R.; Cao, G.; Chen, S.; Zhou, Z.; Yang, Y. Highly mesoporous and high surface area carbon: A high capacitance electrode material for EDLCs with various electrolytes. *Electrochem. Commun.* **2008**, *10*, 795–797. [CrossRef]
46. Wei, J.; Li, Y.; Dai, D.; Zhang, F.; Zou, H.; Yang, X.; Ji, Y.; Li, B.; Wei, X. Surface roughness: A crucial factor to robust electric double layer capacitors. *ACS Appl. Mater. Interfaces* **2020**, *12*, 5786–5792. [CrossRef] [PubMed]
47. Fleischmann, S.; Mitchell, J.B.; Wang, R.; Zhan, C.; Jiang, D.-e.; Presser, V.; Augustyn, V. Pseudocapacitance: From fundamental understanding to high power energy storage materials. *Chem. Rev.* **2020**, *120*, 6738–6782. [CrossRef]

48. Conway, B.E.; Birss, V.; Wojtowicz, J. The role and utilization of pseudocapacitance for energy storage by supercapacitors. *J. Power Sources* **1997**, *66*, 1–14. [CrossRef]
49. Yu, X.; Yun, S.; Yeon, J.S.; Bhattacharya, P.; Wang, L.; Lee, S.W.; Hu, X.; Park, H.S. Emergent pseudocapacitance of 2D nanomaterials. *Adv. Energy Mater.* **2018**, *8*, 1702930. [CrossRef]
50. Liu, Y.; Jiang, S.; Shao, Z. Intercalation pseudocapacitance in electrochemical energy storage: Recent advances in fundamental understanding and materials development. *Mater. Today Adv.* **2020**, *7*, 100072. [CrossRef]
51. Subramanian, V.; Zhu, H.; Vajtai, R.; Ajayan, P.; Wei, B. Hydrothermal synthesis and pseudocapacitance properties of MnO_2 nanostructures. *J. Phys. Chem. B.* **2005**, *109*, 20207–20214. [CrossRef]
52. Chatterjee, D.P.; Nandi, A.K. A review on the recent advances in hybrid supercapacitors. *J. Mater. Chem. A.* **2021**, *9*, 15880–15918. [CrossRef]
53. Muzaffar, A.; Ahamed, M.B.; Deshmukh, K.; Thirumalai, J. A review on recent advances in hybrid supercapacitors: Design, fabrication and applications. *Renew. Sustain. Energy Rev.* **2019**, *101*, 123–145. [CrossRef]
54. Mai, L.-Q.; Yang, F.; Zhao, Y.-L.; Xu, X.; Xu, L.; Luo, Y.-Z. Hierarchical MnMoO4/CoMoO4 heterostructured nanowires with enhanced supercapacitor performance. *Nat. Commun.* **2011**, *2*, 381. [CrossRef] [PubMed]
55. Xu, Y.; Lu, W.; Xu, G.; Chou, T.-W. Structural supercapacitor composites: A review. *Compos. Sci. Technol.* **2021**, *204*, 108636. [CrossRef]
56. Frackowiak, E. Carbon materials for supercapacitor application. *Phys. Chem. Chem. Phys.* **2007**, *9*, 1774–1785. [CrossRef]
57. Snook, G.A.; Kao, P.; Best, A.S. Conducting-polymer-based supercapacitor devices and electrodes. *J. Power Sources* **2011**, *196*, 1–12. [CrossRef]
58. Wang, Y.; Wu, X.; Han, Y.; Li, T. Flexible supercapacitor: Overview and outlooks. *J. Energy Storage* **2021**, *42*, 103053. [CrossRef]
59. Zhang, L.L.; Zhou, R.; Zhao, X. Graphene-based materials as supercapacitor electrodes. *J. Mater. Chem.* **2010**, *20*, 5983–5992. [CrossRef]
60. Amin, K.; Ashraf, N.; Mao, L.; Faul, C.F.; Wei, Z. Conjugated microporous polymers for energy storage: Recent progress and challenges. *Nano Energy* **2021**, *85*, 105958. [CrossRef]
61. Xu, F.; Chen, X.; Tang, Z.; Wu, D.; Fu, R.; Jiang, D. Redox-active conjugated microporous polymers: A new organic platform for highly efficient energy storage. *Chem. Commun.* **2014**, *50*, 4788–4790. [CrossRef]
62. Lee, J.-S.M.; Wu, T.-H.; Alston, B.M.; Briggs, M.E.; Hasell, T.; Hu, C.-C.; Cooper, A.I. Porosity-engineered carbons for supercapacitive energy storage using conjugated microporous polymer precursors. *J. Mater. Chem. A.* **2016**, *4*, 7665–7673. [CrossRef]
63. Lee, J.-S.M.; Cooper, A.I. Advances in conjugated microporous polymers. *Chem. Rev.* **2020**, *120*, 2171–2214. [CrossRef]
64. Liao, Y.; Wang, H.; Zhu, M.; Thomas, A. Efficient supercapacitor energy storage using conjugated microporous polymer networks synthesized from Buchwald–Hartwig coupling. *Adv. Mater.* **2018**, *30*, 1705710. [CrossRef]
65. Yang, L.; Fang, J.; Meichin, N.; Tanaka, K.; Kita, H.; Okamoto, K. Gas permeation properties of thianthrene-5, 5, 10, 10-tetraoxide-containing polyimides. *Polymer* **2001**, *42*, 2021–2029. [CrossRef]
66. Sun, Y.; Yang, X.; Feng, Z.; Liu, B.; Zhong, D.; Zhang, J.; Zhou, G.; Wu, Z. Highly efficient deep-red organic light-emitting devices based on asymmetric iridium (iii) complexes with the thianthrene 5, 5, 10, 10-tetraoxide moiety. *ACS Appl. Mater. Interfaces* **2019**, *11*, 26152–26164. [CrossRef] [PubMed]
67. Li, Z.; Zhang, W.; Wang, H.; Qin, Z. Activated pyrene decorated graphene with enhanced performance for electrochemical energy storage. *Chem. Eng. J.* **2018**, *334*, 845–854. [CrossRef]
68. Bandyopadhyay, S.; Singh, C.; Jash, P.; Hussain, M.W.; Paul, A.; Patra, A. Redox-active, pyrene-based pristine porous organic polymers for efficient energy storage with exceptional cyclic stability. *Chem. Commun.* **2018**, *54*, 6796–6799. [CrossRef]
69. Bachman, J.C.; Kavian, R.; Graham, D.J.; Kim, D.Y.; Noda, S.; Nocera, D.G.; Shao-Horn, Y.; Lee, S.W. Electrochemical polymerization of pyrene derivatives on functionalized carbon nanotubes for pseudocapacitive electrodes. *Nat. Commun.* **2015**, *6*, 7040. [CrossRef]
70. Xue, W.; Mutlu, H.; Li, H.; Wenzel, W.; Theato, P. Structural design of pyrene-functionalized TEMPO-containing polymers for enhanced electrochemical storage performance. *Polym. Chem.* **2021**, *12*, 2643–2650. [CrossRef]
71. Mohamed, M.G.; Chaganti, S.V.; Sharma, S.U.; Samy, M.M.; Ejaz, M.; Lee, J.-T.; Zhang, K.; Kuo, S.-W. Constructing Conjugated Microporous Polymers Containing the Pyrene-4,5,9,10-Tetraone Unit for Energy Storage. *ACS Appl. Energy Mater.* **2022**, *5*, 10130–10140. [CrossRef]
72. Liu, J.; Zhou, Y.; Xie, Z.; Li, Y.; Liu, Y.; Sun, J.; Ma, Y.; Terasaki, O.; Chen, L. Conjugated copper–catecholate framework electrodes for efficient energy storage. *Angew. Chem. Int. Ed.* **2020**, *59*, 1081–1086. [CrossRef] [PubMed]
73. Suzuki, Y.; Yamaguchi, M.; Oketani, R.; Hisaki, I. Isomeric effect of naphthyl spacers on structures and properties of isostructural porous crystalline frameworks. *Mater. Chem. Front.* **2023**, *7*, 106–116. [CrossRef]
74. Sun, Z.-Z.; Feng, S.; Ding, W.-L.; Peng, X.-L.; Guan, J.; Zhao, Z. Molecular design of dibenzo [g,p] chrysene-based hole-transporting materials for perovskite solar cells: A theoretical study. *Synth. Met.* **2021**, *271*, 116631. [CrossRef]
75. Slováková, E.; Zukal, A.; Brus, J.; Balcar, H.; Brabec, L.; Bondarev, D.; Sedláček, J. Transition-Metal-Catalyzed Chain-Growth Polymerization of 1,4-Diethynylbenzene into Microporous Crosslinked Poly (phenylacetylene) s: The Effect of Reaction Conditions. *Macromol. Chem. Phys.* **2014**, *215*, 1855–1869. [CrossRef]

76. Hanková, V.; Slováková, E.; Zedník, J.; Vohlídal, J.; Sivkova, R.; Balcar, H.; Zukal, A.; Brus, J.; Sedláček, J. Polyacetylene-Type Networks Prepared by Coordination Polymerization of Diethynylarenes: New Type of Microporous Organic Polymers. *Macromol. Rapid Commun.* **2012**, *33*, 158–163. [CrossRef] [PubMed]
77. Mohamed, M.G.; Elsayed, M.H.; Elewa, A.M.; EL-Mahdy, A.F.; Yang, C.-H.; Mohammed, A.A.; Chou, H.-H.; Kuo, S.-W. Pyrene-containing conjugated organic microporous polymers for photocatalytic hydrogen evolution from water. *Catal. Sci. Technol.* **2021**, *11*, 2229–2241. [CrossRef]
78. Mei, L.; Cui, X.; Duan, Q.; Li, Y.; Lv, X.; Wang, H.-g. Metal phthalocyanine-linked conjugated microporous polymer hybridized with carbon nanotubes as a high-performance flexible electrode for supercapacitors. *Int. J. Hydrogen Energy.* **2020**, *45*, 22950–22958. [CrossRef]
79. Xu, L.; Shi, R.; Li, H.; Han, C.; Wu, M.; Wong, C.-P.; Kang, F.; Li, B. Pseudocapacitive anthraquinone modified with reduced graphene oxide for flexible symmetric all-solid-state supercapacitors. *Carbon* **2018**, *127*, 459–468. [CrossRef]
80. Goldfarb, J.L.; Dou, G.; Salari, M.; Grinstaff, M.W. Biomass-based fuels and activated carbon electrode materials: An integrated approach to green energy systems. *ACS Sustain. Chem. Eng.* **2017**, *5*, 3046–3054. [CrossRef]
81. DeBlase, C.R.; Silberstein, K.E.; Truong, T.-T.; Abruña, H.D.; Dichtel, W.R. β-Ketoenamine-linked covalent organic frameworks capable of pseudocapacitive energy storage. *J. Am. Chem. Soc.* **2013**, *135*, 16821–16824. [CrossRef] [PubMed]
82. Wan, L.; Wang, J.; Xie, L.; Sun, Y.; Li, K. Nitrogen-enriched hierarchically porous carbons prepared from polybenzoxazine for high-performance supercapacitors. *ACS Appl. Mater. Interfaces* **2014**, *6*, 15583–15596. [CrossRef] [PubMed]
83. Takahashi, R.; Sato, S.; Sodesawa, T.; Nishida, H. Effect of pore size on the liquid-phase pore diffusion of nickel nitrate. *Phys. Chem. Chem. Phys.* **2002**, *4*, 3800–3805. [CrossRef]
84. Ahmed, M.; Imae, T. Effect of external magnetic field on cyclic voltammetry of exfoliated graphene-based magnetic composites with conductive polymer and carbon dots. *J. Magnet. Magnet. Mater.* **2019**, *491*, 165604. [CrossRef]
85. Samy, M.M.; Mohamed, M.G.; Kuo, S.W. Pyrene-functionalized tetraphenylethylene polybenzoxazine for dispersing single-walled carbon nanotubes and energy storage. *Compos. Sci. Technol.* **2020**, *199*, 108360. [CrossRef]
86. Mohamed, M.G.; Hu, H.Y.; Madhu, M.; Samy, M.M.; Mekhemer, I.M.A.; Tseng, W.L.; Chou, H.H.; Kuo, S.W. Ultrastable two-dimensional fluorescent conjugated microporous polymers containing pyrene and fluorene units for metal ion sensing and energy storage. *Eur. Polym. J.* **2023**, *189*, 111980. [CrossRef]
87. Samy, M.M.; Mohamed, M.G.; Sharma, S.U.; Chaganti, S.V.; Lee, J.T.; Kuo, S.W. An Ultrastable Tetrabenzonaphthalene-Linked conjugated microporous polymer functioning as a high-performance electrode for supercapacitors. *J. Taiwan Inst. Chem. Eng.* **2023**, 104750. [CrossRef]
88. Ejaz, M.; Mohamed, M.G.; Sharma, S.U.; Lee, J.-T.; Huang, C.-F.; Chen, T.; Kuo, S.-W. An Ultrastable Porous Polyhedral Oligomeric Silsesquioxane/Tetraphenylthiophene Hybrid as a High-Performance Electrode for Supercapacitors. *Molecules* **2022**, *27*, 6238. [CrossRef]